Chemical Engineering Journal 480 (2024) 147835

Contents lists available at ScienceDirect

Chemical Engineering Journal

journal homepage: www.elsevier.com/locate/cej

Nano-graphitic crystallites effect on the improved K-ion intercalation properties of *Kigelia Africana* fruit-derived hard carbon for potassium-ion batteries

N. Prasanna Naga Puneeth [a], K. Rajkumar [a], A. Soundarya [a], S.D. Kaushik [b], Yun Sung Lee [c], Sangho Park [d], R. Kalai Selvan [a,*]

[a] *Energy Storage and Conversion Devices Laboratory, Department of Physics, Bharathiar University, Coimbatore 641046, Tamil Nadu, India*
[b] *UGC-DAE Consortium for Scientific Research Mumbai Centre, BARC, Trombay, Mumbai 400 085, India*
[c] *Faculty of Applied Chemical Engineering, Chonnam National University, Gwangju 500-757, South Korea*
[d] *Department of Battery Engineering, Dongshin University, Jeollanam-do 58245, Republic of Korea*

ARTICLE INFO

Keywords:
Kigelia Africana
Hard carbon
Nanographitic crystallites
Heteroatom doping
GITT
Anodes for K-ion batteries

ABSTRACT

The development of intermittent renewable energy storage technology is essential for building a sustainable, low-carbon society. Potassium-ion (K-ion) batteries are being extensively explored as alternate energy storage devices due to their closest redox potential and similarities to Lithium (Li) and Sodium (Na) batteries. Identifying alternate carbonaceous materials is, therefore, crucial to overcome the shortcomings of graphite. In this context, hard carbon derived from cellulose-rich *Kigelia Africana* fruit (KAP) was pyrolyzed at 1000 °C and 1100 °C and characterized using various techniques. The employed facile direct carbonization retains the inherent oxygen atoms (6.6 %). It restricts the growth of graphitic crystallites in the *ab* plane, thereby reducing the d-spacing revealed by X-ray Diffraction (XRD) and Raman Spectral analysis. The enhanced K-ion storage through insertion, as corroborated by Cyclic Voltammetry (CV) through the increased kinetics at the low potential < 0.5 V vs K/K^+. The Galvanostatic Charge-Discharge (GCD) analysis further substantiates the role of graphitic nanocrystallites combined with the adsorption of O-atoms through the improved rate capability of KAP-1100 (110 mAh/g at 200 mA/g). On the other hand, KAP-1000 provides 10 mAh/g at 200 mA/g, which is almost ten times lower. Galvanostatic Intermittent Titration Technique (GITT) and Electrochemical Impedance Spectroscopy (EIS) analysis further prove the efficient diffusion coefficient (1.5×10^{-8} cm^2/s) of K-ions in the hard carbon and low charge transfer resistance (R_{ct}). This study reveals the effect of local structure and the inherently available heteroatom for developing better anodes for K-ion batteries.

1. Introduction

The primary consumption of traditional fossil fuels has resulted in environmental pollution and has prompted researchers to focus on tapping the potential of renewable energy resources. On the other hand, the existing renewable energy generation from solar, wind, and other sources is intermittent. Despite the effectiveness of Lithium-ion (Li-ion) battery technology, the implementation cost for large-scale batteries is prohibitive due to the shortage of lithium in the earth's crust. Hence, developing Na and K-ion batteries is necessary for quick and affordable commercialization in grid-scale energy storage to mitigate effectively and balance the intermittency in generating power from renewable sources. Among these, K-ion offers a more comprehensive working potential window close to Li-ion since it has the closest redox potential of −2.97 V vs. SHE with Li^+ ions (−3.01 V vs. SHE). The cheaper aluminum (Al) can also be used as a current collector since there is no alloy formation between K and Al at a lower potential. However, designing low-cost and high-performance anode materials is a big challenge for massive K-ion storage to compete with the existing technologies.

Carbon-based materials like graphite [1], soft carbon [2], and hard carbon with adsorption, intercalation, and pore-filling mechanisms are superior in K-ion storage [3–8] than alloy-based electrodes with conversion mechanism [9,10] and oxides having intercalation processes [11]. The conventional graphite anode suffers structural deterioration

* Corresponding author.
E-mail address: selvankram@buc.edu.in (R.K. Selvan).

https://doi.org/10.1016/j.cej.2023.147835
Received 29 June 2023; Received in revised form 20 November 2023; Accepted 30 November 2023
Available online 27 December 2023

during cycling due to the greater ionic radii of K-ion (1.38 Å) than the Li-ion (0.76 Å), which causes a rapid capacity decay [12]. During insertion, it forms KC_8 with graphite having a theoretical capacity of 279 mAh/g, like LiC_6 in Li-ion batteries (372 mAh/g). During lithiation, $LiC_{32} \rightarrow LiC_{24} \rightarrow LiC_{12} \rightarrow LiC_6$ occurs. At the low voltage region, the SEI layer formation occurs due to lithium plating. On the other hand, $KC_{48} \rightarrow KC_{36} \rightarrow KC_{24} \rightarrow KC_8$ ensues with an intercalation potential higher than Li^+ i.e. < 0.2 V vs. K/K^+ [13,14], which avoids potassium plating that leads to the development of safe K-ion batteries. Despite these advantages, the repeated intercalation of relatively large K^+ ion expands the interlayer spacing of graphite around 10 % than Li^+. This causes the co-intercalation of electrolyte ions into the expanded layers, which leads to low K-ion storage and poor cycling stability [12,15]. Many attempts are being explored to improve the performance by using expanded graphite [16], microcrystalline graphite [14], and functionalized (F-doped) graphite [13]. As well as, amorphous like hard and soft carbon has also been used as the potential anode for K-ion batteries. These hard and soft carbons employ K-ion charge storage via adsorption, pore filling, and K-ion insertion between the nano-graphitic domains [17–19]. Generally, the K-ion adsorption depends on the surface defects/disorderliness, whereas its insertion mechanism depends upon the interlayer(d) spacing, crystallite size, and short diffusion distance. However, specific parameters affecting the formation of the SEI layer at the electrode–electrolyte interface and irreversible loss of K-ions due to insertion are unknown [20].

Synthetic [21] and natural sources [7,22] have been used to prepare hard carbons through direct pyrolysis [23–25], hydrothermal methods [26,27], etc. Among these, hard carbons derived from biomass are highly cost-effective, naturally abundant, have superior electrical conductivity, have the advantage of intrinsic doping [28], and the internal morphology of the biomass serves as a template. The cotton [29,30], walnut septum [31], rice husk [32], loofah [33], potato [34], balsa wood [7], camellia shell [35], orange peels [36], hemp stalks [37,38], bone [39], corn husk [40], Sessile Puffballs [41] (fungus) sugarcane bagasse [42,43], jute fiber [44], ficus religiosa leaf [45], water chestnut [46], bamboo [47], rose petals [48], and pine trees [49] have been used as the source of hard carbon for K-ion batteries. Some works involved energy-expensive techniques and adopted chemical treatment with acids. Despite the attempts, they suffer a significant capacity loss due to SEI formation in the initial cycles. Because of acid and alkali pretreatments, there is a possibility of removing hemicellulose and lignin from the biomasses.

Generally, biomass-derived carbon exhibits different behavior in K-ion storage. Therefore, it is still unclear how the parameters are interdependent in curtailing K-ions. Wu et al. 2019 [33] investigated the alkali-treated loofah-derived hard carbon, which stores K-ion via adsorption due to its highly accessible mesoporous surface and insertion exhibited by the pseudo-graphitic domains with a d-spacing of 3.5 Å, which is larger than graphite. Yang et al. 2021 [26] prepared Ganoderma lucidum spores derived hard carbon in a multistep process with N/O doping (7–8 %) and reported an improved coulombic efficiency from 34 % to 68 % while increasing the degree of disorderness and graphitization (I_D/I_G ratio) from 0.83 to 0.96. Tao et al. 2021 [50] prepared N/P co-doped mesoporous carbon from soybean roots in the facile carbonization method and obtained the high capacity of 197 mAh/g at 2 A/g for 2000 cycles due to the synergistic effect of increased adsorption and the better diffusion of K-ions. Zhao et al. 2022 [51] prepared O-doped orange peel-derived carbon by airflow annealing after carbonization and reported that the oxygen (13.38 %) doping had reduced the adsorption energy for K-ions and C═O bonds promoting the Faradaic reactions on the surface.

In this line, the present work concentrates on preparing hard carbon from *Kigelia Africana* fruit by direct pyrolysis at two different temperatures of 1000 °C and 1100 °C for the first time in K-ion battery applications and explains the K-ion intercalation mechanism. *Kigelia Africana* fruit (KAP) contains 61.5 % cellulose, 12.42 % hemicellulose, and 20 % lignin. Also, 0.66 % of Ca and 0.21 % of Si, and the trace amounts of Na and K [52]. *Kigelia Africana* fruit-derived activated carbon has been used as an adsorbent (Cr, Pb) [53–55], biosorbent [56,57], nanofluids [58], cellulosic fiber [52], etc. The direct pyrolysis method is adopted here since it provides the biomass's collective nature and unique qualities. Similarly, volatile gases produced by biochar during carbonization formed various carbon structures, such as pseudo-graphitic and amorphous disordered regions, as demonstrated by XRD, Raman, and HRTEM investigations. Similarly, cellulose is rich in hydroxyl linkages, which aids in inherently synthesizing hard carbon with oxygen defects, as confirmed by XPS analysis. Finally, the K-ion intercalation/deintercalation behavior is studied, and the mechanism is explained based on the above observations.

2. Experimental methods and materials

Kigelia Africana (KA) fruit was collected from Kalveerampalayam (11.0277° N, 76.8840° E), Bharathiar University Campus, Coimbatore, India. It was washed thoroughly with double distilled water, cut into small pieces, and sun-dried. The dried pieces of KA fruit were milled into powder. The milled powder was calcinated at 1000 and 1100 °C for two hours at 5 °C/min under an N_2 atmosphere. The carbonized powder was subjected to pickling in 2 M HCl for 12 h to remove all the inorganic impurities. Then, it was washed thoroughly in water and ethanol multiple times and dried in a hot air oven at 100 °C for 24 h. A schematic representation is shown in Fig. S1. The carbonized KA fruit-derived carbon at 1000 and 1100 °C are denoted as KAP-1000 and KAP-1100, respectively, hereafter.

The structural analysis of the prepared carbon was carried out with the X-ray Diffractometer (Malvern PANalytical - Empyrean, Cu Kα – 1.5418 Å). The powdered sample was evenly spread on the silica holder to fill the cavity with a depth of 1 mm and a diameter of 16 mm with the help of a glass plate. The powder XRD pattern was obtained between $2\theta = 10 - 80°$ with a step size of 0.026°. The FTIR analysis was performed using JASCO FT/IR-4700 type A in the ATR mode at the incident angle of 45°. The data was acquired at an interval of 0.964 cm^{-1} in the 500 – 4000 cm^{-1} range. Raman Spectral data were obtained using JASCO NRS-5100 series confocal Raman Microscope at an interval of 1 cm^{-1} employing a monochromatic LASER with wavelength 532 nm and power 1.3 mW. BET analysis with Mircomeritics ASAP2020 N_2–adsorption–desorption isotherm at 77 K. The samples were degassed at 150° C for 12 hrs prior to measurement. The surface area was calculated using the Brunauer-Emmett-Teller (BET) method, and pore size distribution was determined using the Barrett-Joyner-Halenda (BJH) method for mesoporous. The X-ray photoelectron spectrometer (XPS Axis Ultra, Kratos Analytical, UK) with monochromatized Al Kα ($h\nu = 1486.6$ eV) was utilized to determine the surface compositions of the prepared carbon. The samples were placed on the holder using carbon tape (Ted Pella-16073). The scan area was 300 × 700 μm with a dwell time of 250 ms and step size of 1000 meV. High-resolution transmission electron microscopy (HR – TEM, JEOL TEM 2100 plus) images and SAED patterns were obtained from the sample coated onto the Cu grid after dispersion in D.D. water.

The negative electrodes are prepared by mixing the active material, carbon black (Sigma Aldrich), and poly(vinylidene) fluoride (PVdF purchased from Sigma Aldrich) in 80:10:10 wt % with the required amount of N-methyl-2-pyrrolidone (NMP, sigma Aldrich, > 99.0 % purity) by doctor blade technique. The prepared slurry was coated onto a carbon-coated aluminum foil to form an electrode tape, which was dried at 90 °C overnight in a vacuum. This electrode tape was punched into 12 mm discs. The coin cell was assembled in the glove box ($H_2O < 0.5$ ppm, $O_2 < 0.5$ ppm) with the KAP carbon as the working electrode and K metal (Sigma Aldrich) as the counter electrode with 0.8 M KPF_6 (Potassium hexafluorophosphate, Sigma Aldrich, > 99 %) in EC (Ethylene Carbonate): DEC (Diethylene Carbonate) (1:1, v:v %) (Sigma Aldrich) separated by a glass fiber in a CR 2032 coin cell.

3. Results and discussion

3.1. Structural analysis

Fig. 1a shows the powder X-ray diffraction (XRD) pattern of the KAP-1000 and KAP-1100, and the observed two broad prominent peaks centered at 23° and 43° correspond to (002) and (100) planes, respectively. A slight peak shift was observed for the (002) plane while increasing the carbonization temperature from 1000 to 1100 °C. Similarly, the peak shape of the (002) plane of KAP-1000 is asymmetric from the center, whereas it is symmetric in KAP-1100. The calculated interlayer spacing (d_{002}) decreases from 3.74 to 3.71 Å as the temperature increases from 1000 to 1100 °C, larger than graphite (3.36 Å) along the c-axis. This larger d-spacing benefits the de-intercalation/intercalation of K-ions [1,15,16]. The observed d-spacing confirms the formation of hard carbon; generally, it lies between 3.7 - 4.2 Å along the (0 0 2) plane [59].

Generally, XRD describes the collective microstructure and provides information about graphitic domains and the degree of disorderness in the carbon samples. Therefore, the parameters like the R-factor, the average thickness (L_c), and the average width of the nanocrystalline domains (L_a) along the *ab*-plane and the number of stacked graphene layers (N) are calculated (Table S1**)** [60,61] using Scherrer equations (eqn. 1–3) to have a clear quantitative understanding of the prepared carbon.

$$L_c = \frac{0.89\lambda}{\beta\cos\theta} \quad (1)$$

$$L_a = \frac{1.84\lambda}{\beta\cos\theta} \quad (2)$$

$$N = \frac{L_c}{002} \quad (3)$$

The calculated empirical R-value [62,63] of KAP-1000 is 1.9, and KAP-1100 is 2.4. This indicates that the high-temperature treatment transforms chaotic disordered turbostratic domains into pseudo-graphitic domains by locally aligning the multi-layered graphene sheets. On the other hand, no significant changes were observed for L_α and L_c because the cross-linking of the constituents in the biomass doesn't affect the growth of the graphitic crystallites at higher carbonization temperatures. However, this turbostratic domain experiences a relative ordering that decreases the d-spacing and nanographitic domains. Further, the obtained number of layers (N) stacked along the c-axis matches the reported hard carbon of 2—6 layers [20]. Overall, the KAP-1100 has a higher degree of graphitization and local ordering with nanographitic domains than the KAP-1000, which is responsible for the adsorption of K- ions. Likewise, the graphitic layers are believed to contribute to charge storage by storing K-ions between their graphenic layers.

FT-IR spectral analysis (Fig. S2) is used to identify the functional groups present in the prepared hard carbon. The FT-IR spectra evidenced the formation of oxygen defects in disordered carbon through cellulose, hemicellulose, and lignin decomposition during carbonization. The observed bands at 1249 and 1228 cm^{-1} reflect the unique modes of O═C-OH, and the weak band at 1774 cm^{-1} indicates C═O stretching [64,65]. Further, the 2983 and 2903 cm^{-1} bands infer the –CH and $–CH_2$ stretching vibrations [66]. The out-of-plane bending of the C-H bond is obtained at 900 cm^{-1} [67,68]. The weak bands at 3670 cm^{-1} and 1406 cm^{-1} illustrate the stretching and vibration modes of –OH vibrations [65]. The observed strong -C-H and CH_2 bonds revealed the partial graphitization of KAP-1000 and KAP-1100 due to the strong interaction between the cellulose, lignin, and hemicellulose without any pretreatments of the raw materials [67]. The available strong O═C-OH bonds indicate the presence of surface and edge functionalized oxygen groups derived from the rich cellulose [69,70]. Overall, the cross-linking between the constituents highly influences the degree of graphitization during direct carbonization and the relative decrease in intensities of KAP-1100 than in KAP-1000, indicating a disordered domain rich in O-atom.

Further, the BET analysis determines the specific surface area, pore distribution, and pore volume measured from 0 to 1 of P/P_0. Fig. 1b suggests that the observed adsorption/desorption isotherm is type IV, with the hysteresis loop in the region between 0.4 and 0.9 P/P_o. The calculated specific surface area is 4.1 and 5.2 m^2/g for KAP-1000 and KAP-1100, respectively. The slight increase in surface area with carbonization temperature is attributed to the direct carbonization of biomass without pretreatment, which results in the degradation of organic matter such as cellulose, lignin, and hemicellulose into C_2H_4, CO_2, and CO [27]. Like surface area, the pore volume also increased to 0.0129 from 0.0121 cm^3/g for KAP-1100 and KAP-1000, respectively, indicating a slightly higher pore volume at high temperatures [71,72]. The observed pore size distribution (Fig. S3) reveals the distribution of micropores in KAP-1100 and KAP-1000 are 0.8–1.4 nm and 0.8–1.6 nm, respectively, with an average pore size of 0.9 and 1.2 nm. The reduction of functional groups, an inadequate buildup of C-C aromatic structures with an increase in the spinning graphene layers, and volatilization of light organic substances cause micropores [67,73,74]. These micropores are also conducive to the transport of electrons and ions. Further, the BET results substantiate the local ordering of carbon contributing to the intergranular porosity since the rearrangement of the carbon structure strongly affects the size of the pores and the pore volume. As well as the increased pore size formation causes the weaker coordination, which was suppressed at high temperature for KAP-1100 with increased concentration of sub-micropores.

The turbostratic nature of graphitization was investigated using Raman spectroscopy for KAP-1000 and KAP-1100 (Fig. 2a and 2b). The strong peaks at ~1348 cm^{-1} and ~1591 cm^{-1} represent the disordered/

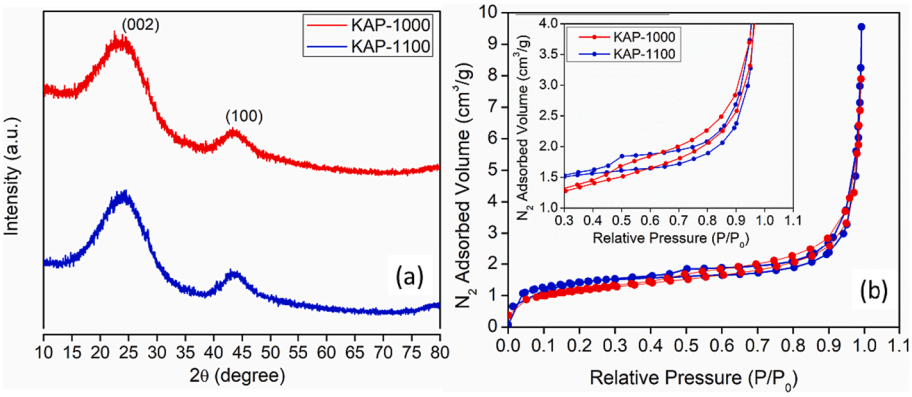

Fig. 1. (a) XRD analysis and (b) N_2 adsorption and desorption curves of the prepared hard carbon.

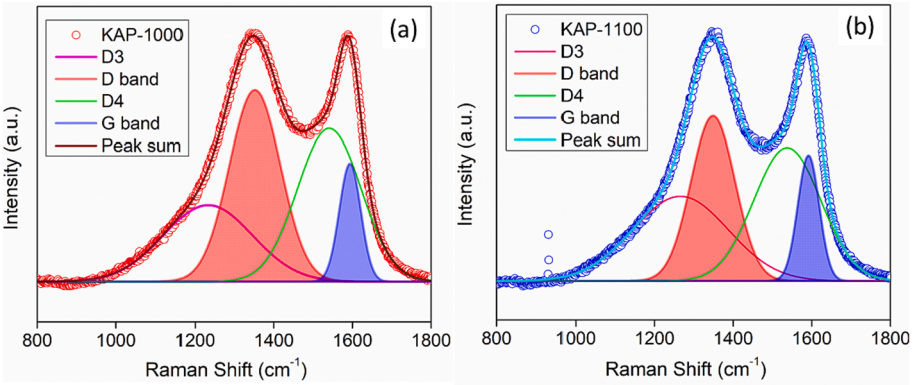

Fig. 2. The de-convoluted Raman spectra of (a) KAP-1000 and (b) KAP-1100.

defective (D band) and graphitic structure (G band), respectively. The D band corresponds to the A_{1g} phonon mode vibrations of the sp^3 domains, and the G band corresponds to the sp^2 crystalline graphene sheets for the first-order Raman scattering from the E_{2g} phonon mode vibrations [1]. The presence of the D band relates to the relaxing sp^2 rings and chains. The peak intensity ratio of the D and G bands (I_D /I_G) reflects the degree of graphitic ordering, which is around 1.6211 and 1.3134, calculated from the respective peak intensities. It suggests the existence of fewer

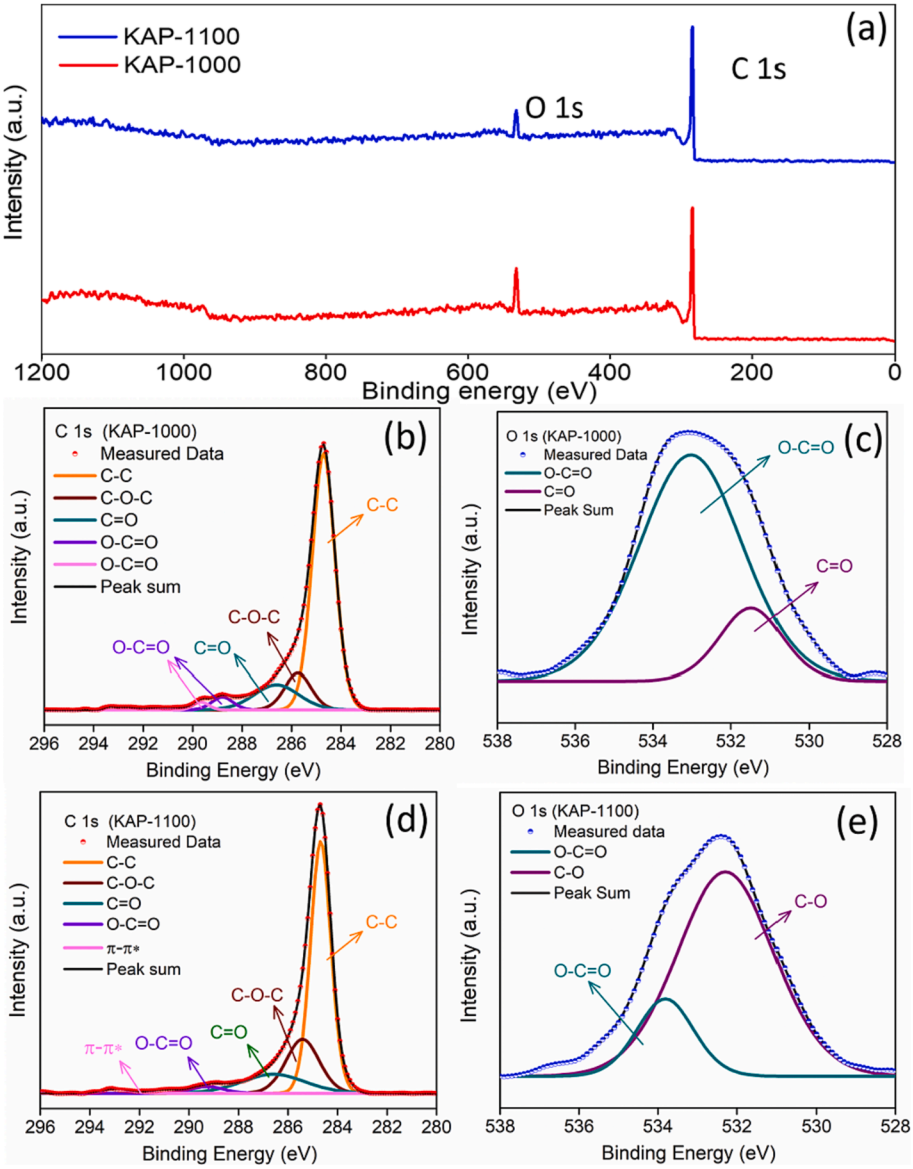

Fig. 3. (a) XPS survey spectra and de-convoluted (b) C 1s & (c) O 1s spectra of KAP-1000 and (d) C 1s & (e) O 1s spectra of KAP-1100.

defects and minor structural deformation in the KAP-1100.

Further, the de-convoluted Raman spectra elucidated four components of G, D, D_3, and D_4 corresponding to the sp^2, sp^3, C-H, and amorphous nature, which provides more insight into the prepared carbon [74,75]. Here, D denotes the microcrystalline nature of the graphite or the disordered graphitic lattice [76,77]. Specifically, D_3 and D_4 infer the presence of large amounts of amorphous carbon with C-H terminating groups. The de-convoluted peaks represent the stretching of C-C/C═C at 1266 cm^{-1}. In addition, the I_{D4}/I_G ratio estimates the amount of $sp^3 - sp^2$ hybridization defect, which shows an increase in graphitization with the corresponding change in edge functional defect groups with more edge defect groups [78]. The full-width half maximum (FWHM) and the integral ratio of the area under narrow G and broad D bands (A_G/A_D) (Table S3) indicate that the lateral graphene is highly defective. In addition, the observed second order and combinational overtone at ~2750 cm^{-1} revealed the 2D and 2G bands, which denotes the multilayer graphitic nature of KAP, as shown in Fig. S5. The calculated 2D /2G ratio is 1.015, similar to the (I_D /I_G), which substantiates the structural growth of multilayer graphene sheets as observed in the XRD.

Further, the nanocrystallite size (L_α) along the *ab* plane is calculated using equation 4 and is 5.0 nm for KAP-1000 and 7.1 nm for KAP-1100.

$$L\alpha(nm) = (2.4 \times 10^{-10})\lambda^4 \left(\frac{A_G}{A_D}\right) \quad (4)$$

where λ denotes the LASER wavelength (532 nm), A_G and A_D are the integrated areas of the fitted D and G bands. The obtained L_α shows that the formed graphitic nanocrystallites are increased, substantiating the I_D/I_G ratio [79–81]. The I_D/I_G ratio does not necessarily indicate the structure's defects. While interpreting the I_D and I_G band, the graphitic nanocrystallite size needs to be considered since the crystallite size is < 20 Å in the present case. Even though the XRD pattern elucidated the macrostructure, the Raman analysis provides more detailed local structural changes. A D-mode vibration is also attributed to increased structural ordering and defect density [4,82]. Likewise, the deconvolution of the Raman Spectra has inferred the presence of an excess number of defects in the KAP-1000 relative to the KAP-1100. Overall, the KAP-1000 has lower graphitization than the KAP-1100, demonstrating the microcrystalline nature of carbon nano-domains.

Fig. 3a shows the survey spectra of the KAP-1000 and KAP-1100 samples, which exhibit two distinguished peaks at 284 eV and 532 eV corresponding to C1s and O1s, respectively, without any impurities. The de-convoluted C 1s spectra of both KAP-1000 and KAP-1100 (Fig. 3b and 3d) revealed the peaks at 284.7, 285.7, 286.6, and 288.8 eV corresponding to the C═C, C-O-C, C-O, and O-CO, respectively [83]. While increasing the carbonization temperature, the peak at 288.8 and 292.6 eV in KAP-1000 converted into a single broad peak centered at 289.2 eV in KAP-1100. Further, the observed small shake-up peak at 292 eV in KAP-1100 indicates the presence of $\pi - \pi^*$, which is responsible for better electronic conductivity of sp^2 carbon [65,84]. Also, oxygen concentration decreased from 10.8 % to 6.6 % while increasing the carbonization temperature, which was determined using the relative sensitivity factors (RSF) [85,86].

The de-convoluted O 1 s spectra are shown in Fig. 3 (c and e). The observed peaks at 531.4 eV and 533.85 eV correspond to the C═O and O-C═O [87–89] for KAP-1000. On the other hand, the KAP-1100 provides peaks at 532.1 eV and 533.85 eV, corresponding to C-O and O-C═O bonds, respectively. The shift in the energy from 531.4 eV to 532.1 eV while increasing the carbonization temperature corroborated the decrease in oxygen percentage and the redistribution of C═O bonds into rich C-O defects [90]. The intensity of the O-C═O bonds at 533.85 eV also decreased drastically. This is in accordance with the broadening for O-C═O observed in C 1s. Therefore, the high-temperature carbonization has prominently mitigated the oxygen and modified the nature of defects on the surface. Subsequently, this also triggered the local ordering of carbon atoms, which initiated the occurrence and improved formation of nano-graphitic crystallites as observed from $\pi - \pi^*$ bonds in KAP-1100. These changes collectively support the improved graphitization degree observed in Raman and XRD analysis.

3.2. Microstructural analysis

The HRTEM analysis (Fig. 4) was employed to understand the microstructural analysis, especially the local ordering in KAP-1000 and KAP-1100. The HRTEM image of KAP-1000 (Fig. 4a) shows the initiation of pseudo-graphitic domains at 1000 °C. Figure 4 (b-d) further revealed the transformation/evolution of the turbostratic domain (indicated by curvy yellow lines) into pseudo-graphitic stacked crystallites (yellow lines) by forming lattice fringes as the carbonization temperature increases to 1100 °C (KAP-1100). The typical d-spacing of the pseudo-graphitic domains was obtained from 3.6 to 4.2 Å of breadth 2.5 nm. On the other hand, the nano-graphitic domains has approximately two layers which are randomly oriented in KAP-1000 [91]. These domains are mainly found around the edges and in the interior of the KAP-1000 particles. The spherical dots towards the interior of the particle are present majorly around the yellow circles in KAP-1000, indicating the amorphous domains.

Further, KAP-1100 (Fig. 4(b-d)) shows the formation of better nano-graphitic domains, as marked in yellow circles. The domains are ordered with large numbers, and the twisted Graphenic domains of 2–5 nm with smaller d-spacing were observed. The change in disorderness and variation towards graphitization of curved graphitic turbostratic domains can be seen more than in KAP-1000. Also, the SAED pattern for KAP-1000 and KAP-1100 (Inset: Fig. 4a,b) shows the diffused ring with no diffraction spots that implied the amorphous structures and short-range ordering (lower degree of graphitization). The randomly oriented graphene sheets and pseudo-graphitic domains are observed at 1100 °C along with the increased spherical dots in KAP-1100 [92]. This further corroborates the observations of graphitization degree by calculating crystallite size from XRD and Raman analysis. The reduced amorphous domains further affirm the volatilization of the small molecules, as observed from BET analysis. Therefore, it can be confirmed that the temperature could not provide sufficient energy to initiate graphitization in KAP-1000. The 2 nm scale HR-TEM images in Fig. 4c and 4d of KAP-1100 show the curvy lattice fringes indicative of the transformation of disordered carbon into pseudographitic nature due to the local ordering. The voids and the restriction of lattice fringes indicate the pore formation and the growth of the pseudo-graphitic nanocrystalline domain along the edges of the pores into the structure.

3.3. Electrochemical analysis

The cyclic voltammetry was performed in the potential range of 0.01–3.0 V vs. K/K^+ at a scan rate of 0.05 mV/s to demonstrate the K-ion storage mechanism of KAP-1000 and KAP-1100. The first two cycles of the CV curve of KAP-1000 and KAP-1100 are shown in Fig. 5. In the first cycle, the cathodic scan exhibits three peaks. The irreversible peak at 1.25 V vs. K/K^+ indicates the SEI layer formation due to the interaction of the electrolyte with the electrode surface. The peaks at 0.75 V and 0.2 V vs. K/K^+ correspond to the formation of KC_{16} and KC_8 by intercalating the K-ions into the carbon layer, respectively [69]. Subsequently, the anodic scan exhibited peaks corresponding to K-ion extraction from the disordered carbon at 0.16 V and 0.31 V vs. K/K^+. Similar redox peaks were observed in the cellulose-rich and lignin-derived hard carbon due to the formation of KC_8 [1,69,93]. The peak at 0.75 V vs. K/K^+ diminishes upon cycling after the formation of stable SEI. The observed reduction peak at ~0.5 V vs. K/K^+ elucidates the adsorption of K^+ ions on the surface O atoms [51,77]. The region below 0.25 V vs. K/K^+ infers the intercalation of K^+ ions. The oxidation peak above 0.40 V vs. K/K^+ corresponds to removing adsorbed K^+ ions from the carbon surface. On cycling, the overlap of redox peaks below 0.5 V

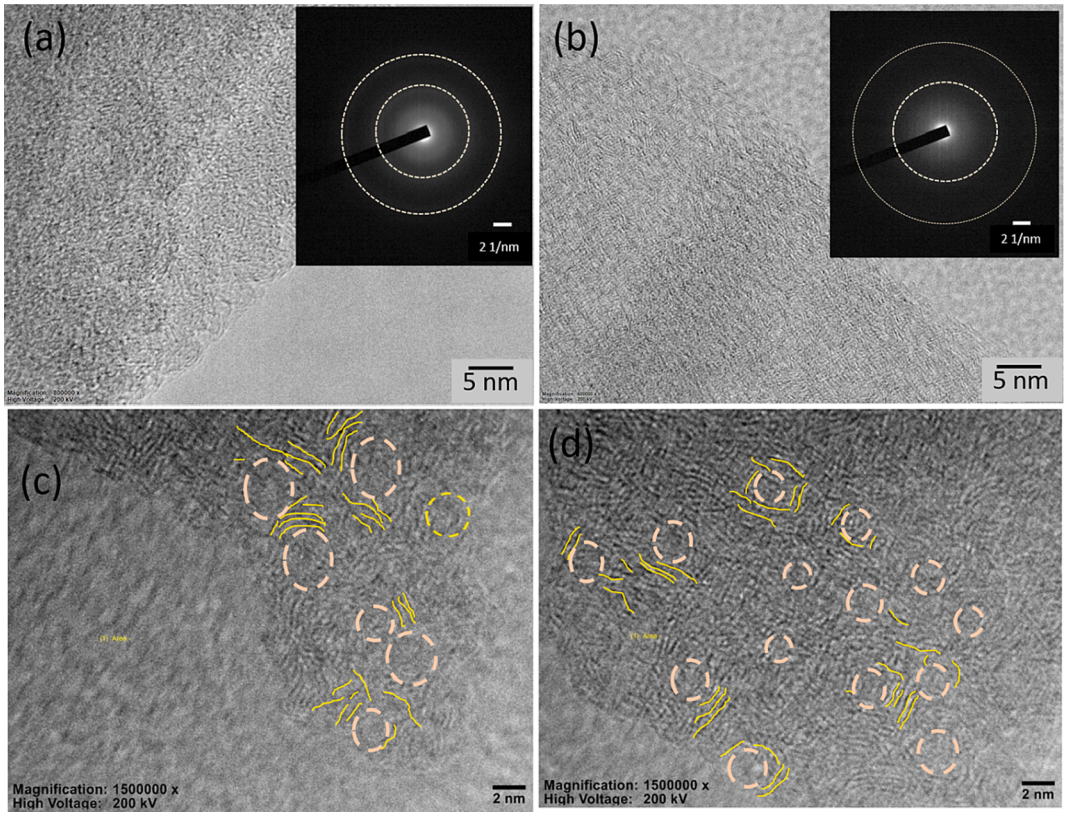

Fig. 4. HR-TEM image of (a) KAP-1000 and (b-d) KAP-1100 (inset: corresponding SAED pattern). The light orange dashed circles and curvy yellow lines indicate the pores and turbostratic pseudographitic crystallites of KAP-1100, respectively. (For interpretation of the references to colour in this figure legend, the reader is referred to the web version of this article.)

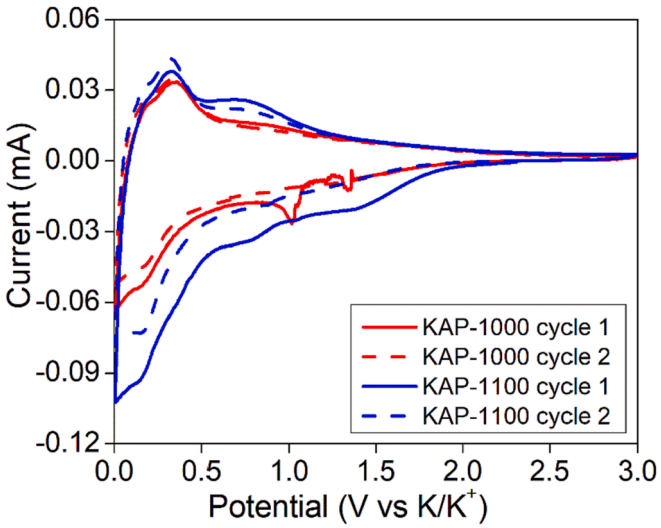

Fig. 5. Cyclic voltammogram at 0.05 mV/s for KAP-1000 and KAP-1100.

vs. K/K^+ demonstrates the reversibility of the charge storage[16].

Further, the cyclic voltammogram was measured at various scan rates from 0.05 to 10 mV/s to investigate the K-ion storage mechanism (Fig. 6). The redox peaks in the region below 0.5 V vs. K/K^+ (Fig. 6 (a and c), elucidate that the charge storage is predominantly due to the insertion mechanism. The KAP-1100 electrode contributed more current area through the diffusion-controlled K-ion insertion due to the availability of a more graphitic region.

On the other hand, no redox peaks were observed at higher scan rates (Fig. 6 (b and d)), and the rate of increase in current was different at slow scan rates (0.05 – 0.5 mV/s). The charge storage mechanism was investigated using the Power law (eqn. 5), and the results are given in Fig. 7a.

$$I = a\nu^b \quad (5)$$

where, I is the peak current (I), ν is the scan rate (mV/s), a and b are the constants. The constants a and b are derived from the slope, plotting between the log (ν) vs. log (i). If b = 0.5, the process is diffusion-controlled (Faradaic), where the ion insertions occur into the bulk and pores [94]. If b = 1, the charge storage occurs at the surface/surface functionalized heteroatoms [26]. In the present case, the obtained b-value for KAP-1000 is 0.76, and KAP-1100 is 0.66, with an excellent linear relationship ($R^2 = 0.986$). The b-values indicate the occurrence of both diffusive and pseudocapacitive reactions during charge storage [26]. However, the obtained b-value is closer to the average of 0.75, where the region lies between the diffusive and capacitive regions. Therefore, Dunn's method is employed to investigate further the individual contribution and the detailed insight mechanism [7].

It is well known that the pseudocapacitive and diffusion current is directly proportional to scan rates and the square root of the scan rates. Therefore, the CV current is the summation of the current contribution of pseudocapacitive and diffusion-controlled. It can be expressed as equation (6) [7],

$$I = k_1 \nu + k_2 \nu^{1/2} \quad (6)$$

where k_1 and k_2 are the constants. At any given voltage, the observed current reflects their respective contributions. The capacitive and diffusive contribution was calculated (Fig. 7b) by resolving the observed current using Dunn's method. The diffusion-controlled contribution of KAP-1100 is 78.34 % at 0.05 mV/s and 46.55 % at 1 mV/s. Whereas

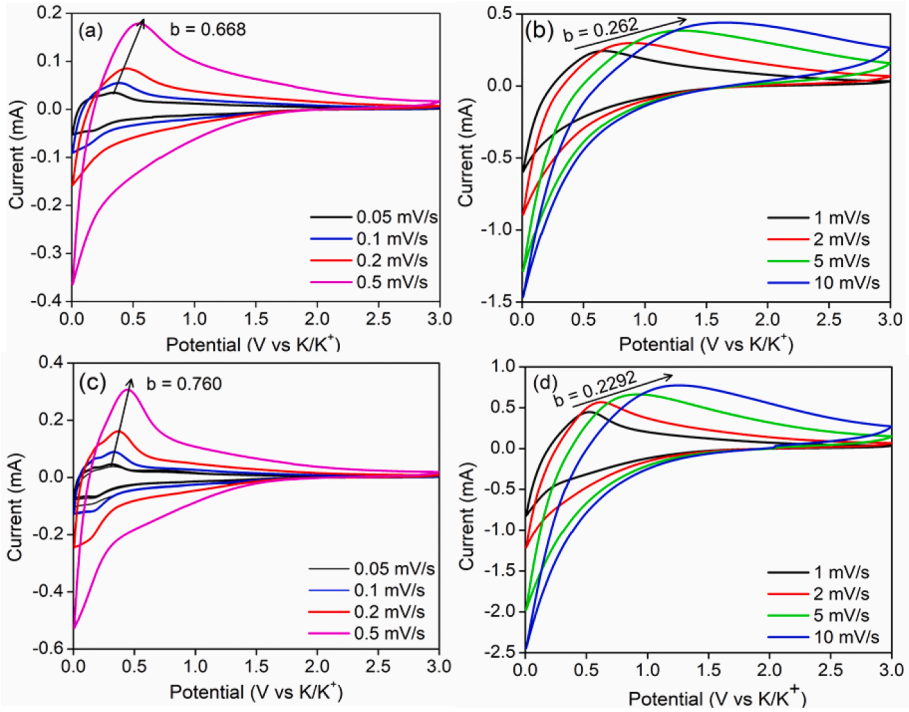

Fig. 6. Cyclic voltammograms of (a, b) KAP-1000 and (c,d) KAP-1100 at different scan rates.

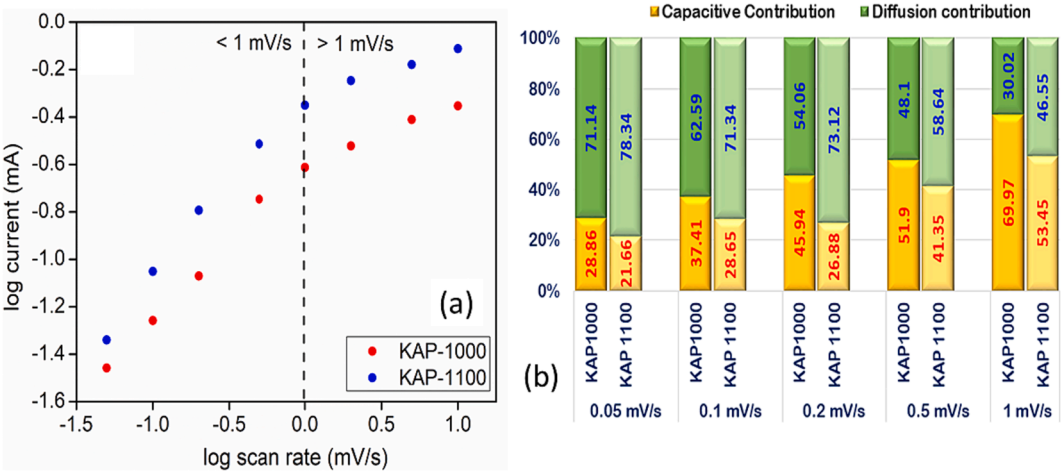

Fig. 7. (a) Power law (b) Contribution of capacitive and diffusion-controlled processes at 0.05–1 mV/s of KAP-1000 and KAP-1100.

71.14 % were at 0.05 mV/s, and 30.02 % were at 1 mV/s for KAP-1000. The observed larger diffusion contribution in KAP-1100 at a higher scan rate (1 – 10 mV/s) is due to the change in the degree of disorderedness [6,91]. Further, the area under the CV curves is large at higher scan rates (Fig. 6b, d), representing the contribution solely of pseudocapacitive nature.

Subsequently, the diffusion coefficient of K-ions was calculated using Randel Sevick's equation (eqn. 7). The plot of the square root of the scan rate vs peak current graph is shown in Fig. S6. Comparatively, the peak current increasing rate is low at a higher scan rate (above 1 mV/s), which is dominated by the surface adsorption mechanisms. On the other hand, a linear increase in peak current is observed below 1 mV/s due to the insertion mechanism of K-ions. The calculated diffusion coefficient below 1 mV/s is 15.73 × 10^{-8} cm^2/s for KAP1000 and 3.705 × 10^{-8} cm^2/s for KAP1100 [6].

$$I_p = 0.4463NFAC\left(\frac{nFvD}{RT}\right)^{1/2} \quad (7)$$

where n is the no. of electrons transferred in the redox process (n = 1/8) [1,15], A is the area of the electrode–electrolyte interface (A = 1.13 cm^2), F is Faraday constant, C is the concentration of K-ions (mol/cm^3)(C = 0.0008 mol/cm^3), R – gas constant and T is the temperature, D is diffusion coefficient of K ions in cm^2/s.

Unfortunately, the KAP-1000 provides a larger ionic diffusion coefficient since it contains more micropores and the O-atoms at the surface, which is confirmed by the observed higher capacitive current (Fig. 7b) [95]. On the other hand, the structural ordering occurs at 1100 °C, where the disordering in the edge defects and the pores are reduced, which gives more room for the interaction of the K- ion with surrounding carbon atoms. So, the K-ion adsorption on the surface and surface induction improve the kinetics and increase the capacitive contribution

since the formation of SEI is dominated by C-O. In contrast, the highly conductive K_2CO_3 promotes/forms the thin layer of SEI. Hence, the increase in temperature modified the bonding of O with the carbon atom with a high decrease in C═O and compensated by the C-O. As observed in the BET analysis, the effective surface area of the prepared hard carbon is less due to the inability to convert cellulose and hemicellulose into graphitic carbon entirely. However, KAP-1100 provides a higher surface area and oxygen (as observed in the XPS analysis) hard carbon with a high pseudo-graphitic domain, leading to a comparatively pseudocapacitive contribution.

Fig. 8 (a, b) and S5a show the GCD curves of the KAP-1000 and KAP-1100 electrodes measured at different current densities in the potential range between 0.01 and 3 V vs. K/K^+. The discharge profile has both steep/slopy and plateau regions. Typically, the steep region in the voltage range 1.5–0.5 V vs. K/K^+ corresponds to the K-ion adsorption on the surface of the active electrode. Meanwhile, the plateau region, between 0.5 and 0.01 V vs. K/K^+, corresponds to the intercalation of K^+ ions into pseudo-graphitic layers and the filling of micropores of the hard carbon. In the present case, the obtained normalized discharge curve (Fig. S7) reveals the slopy profile in KAP-1000. In contrast, both slope and plateau regions were observed in KAP-1100 [91]. It elucidates that the charge contribution in K^+-ion storage is highly capacitive in KAP-1000 and almost equally via insertion and adsorption of K-ions in KAP-1100 at low discharge voltages. The first discharge and charge capacities of KAP-1100 are 547 & 230 mAh/g. The initial coulombic efficiency (ICE) of KAP-1100 was 42.3 %, and KAP-1000 was 32 %. The irreversible capacity arises due to the formation of the SEI layer. In the subsequent cycles (Fig. S7), the coulombic efficiency gradually increased to 95 %. Further, the rate capability performances of the prepared KAP-1000 and KAP-1100 electrodes at different current densities are shown in Fig. 8c. Among these, the KAP-1100 demonstrated better reversible specific capacities of 220, 180, 160, 110, 68, and 32 mAh/g at 20, 50, 100, 200, 500, and 1000 mA/g, respectively. Again, when cycled back at 20 mA/g, it exhibited a capacity of 182 mAh/g with a capacity retention of 82.7 %. Interestingly, KAP-1100 provided a higher discharge capacity of 110 mAh/g at 200 mA/g (Fig. 8b). On the other hand, the rate capability of KAP-1000 shows a severe capacity fading upon cycling until 200 mA/g (Fig. 8c) since there is no extended plateau region (marked in Fig. 8a) while current densities increase. Therefore, it delivered only 10 mAh/g discharge capacity at 200 mA/g due to decreased K-ions during reversible insertion.

Using the GCD profile (Fig. 8a and b), the contribution of adsorption (>0.5 V vs. K/K^+) and insertion (<0.5 V vs. K/K^+) behavior is explained by calculating the plateau capacity and slope capacity (Fig. 8d and S7). The slight but proportional decrease in the plateau capacity with increasing current densities is observed for KAP-1100 (Fig. 8d), whereas KAP-1000 (Fig. S8) shows relatively poor kinetics in the low voltage, causing a quick fade exhibiting a capacity of 44 mAh/g, unlike KAP-1100 with 140 mAh/g at a current density of 100 mA/g. Interestingly, KAP-1100 retained 83.7 % of its initial capacity upon cycling even after 200 cycles at a higher current density of 200 mA/g (Fig. 8e). Therefore, it is understood that the local ordering significantly facilitates the migration pathways for K-ions through the nanographitic domains in KAP-1100. Overall, the low d-spacing of KAP-1100, the layer-to-layer coherency in the randomly oriented graphenic layers determined from the R factor using the (002) plane, relatively high graphitization from the integrated intensities of the D and G band, and the curved and interconnected graphenic domains supporting the observed improved kinetics for feasible insertion of K-ions. Larbi et al. [85] investigated the hard carbon derived from resin spheres and exhibited a cyclic stability of 79–88 % after 50 cycles. Liu et al. [96] employed hard carbon derived from hypercrosslinked polymer and attained 83.2 % capacity retention at 50 mA/g. Further, the mixed biomass has demonstrated a decay of 0.147 % after 1000 cycles due to the presence of N, P, and S in the carbon spheres derived from single glucose [97]. Besides synthetic precursors, Wu et al. [6] investigated the K-ion storage of lignin with varied molecular weight and carbonization temperatures and reported a capacity retention of 80 % even after 100 cycles. Therefore, temperature, surface chemistry arising from the functional groups, specific surface area, and interplanar spacing collectively affected the

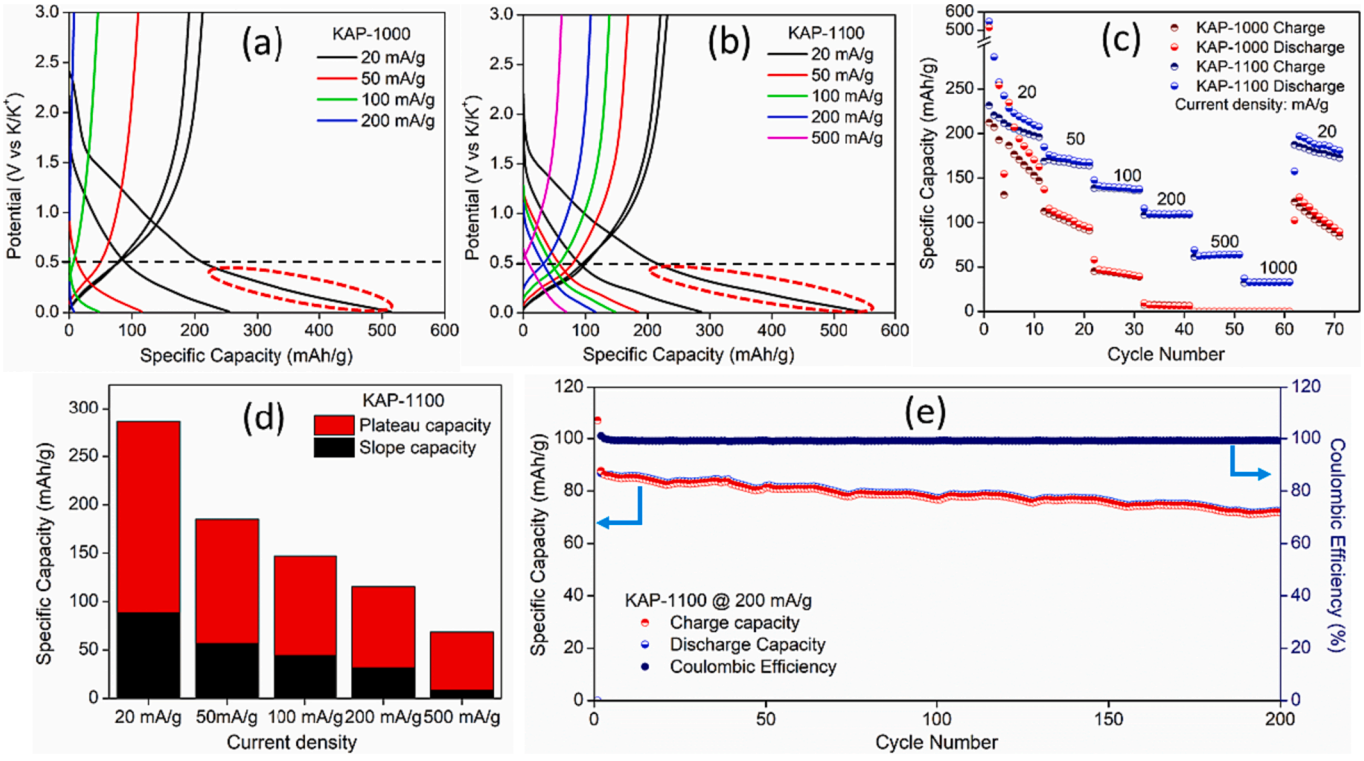

Fig. 8. (a-c) The galvanostatic charge-discharge profile and the rate capability of KAP-1000 and KAP-1100. (d) The calculated capacity contribution of KAP-1100 and (e) the cycling stability of KAP-1100 at 200 mA/g.

electrochemical performance (Table 1). Considering the cost-effectiveness, the naturally occurring lignin, hemicellulose, and cellulose in biomass are considered quite economical and eco-friendly.

Electrochemical Impedance Spectroscopy (EIS) analysis was conducted to study the charge transfer properties of the K-ion cells (Fig. 9a). The EIS spectra were fitted through an equivalent circuit constituting the R_s and R_{ct} corresponding to ohmic and charge transfer resistance. It is well known that the x-intercept in the EIS represents the ohmic resistance (R_s) of the current collector and the active material. This is followed by a semicircle in the mid-frequency region, arising from the charge transfer resistance and the solid electrolyte interface (SEI) of the KAP carbon and the electrolyte. A Warburg region in the low frequencies corresponds to the constant phase element (CPE) for the double-layer formation. The fitted parameters are given in Table S5, where the R_{ct} of KAP-1100 shows increased charge transfer resistance. [51]. When the temperature is increased from 1000 °C to 1100 °C, the effect of change in the domains of disorderness to pseudographitic domains leads to a relatively high charge transfer resistance for the migration of K-ions.

The real part of impedance was calculated from equation (8) [103,104].

$$Z' = R_s + R_{ct} + \sigma\omega^{1/2} \tag{8}$$

here Z' is the real impedance, R_s is the solution resistance, R_{ct} is charge transfer resistance, and ω is the angular frequency, σ is calculated from the plot in Fig. 9b. Further, the kinetics of the K^+ diffusion coefficient (D_K^+) was calculated from equation (9)

$$D_{K^+} = \frac{R^2T^2}{2A^2n^4F^4C_K{}^2\sigma^2} \tag{9}$$

where R- gas constant, T is absolute Temperature in K, A is the surface area of the electrode in cm^2, n is the number of electrons, F is Faraday's constant, C_K concentration of K-ions, and σ is the Warburg Coefficient. The calculated values are 0.317×10^{-9} cm^2/s for KAP-1000 and 1.154×10^{-9} cm^2/s for KAP-1100. The initial kinetics are faster for KAP-1100, with a relatively high diffusion coefficient.

GITT analysis was performed to understand further the charge storage mechanism in the porous and the intercalation of K-ion in the anode. During the GITT measurements, the constant current pulse was applied for 20 mins at 10 mA/g and left at the open potential for 2 hrs to reach equilibrium potentials throughout the charge–discharge. Fig. 10 (a,b) shows the GITT analysis of KAP-1000 and KAP-1100 measured at 10 mA/g.

Based on Fick's second law, the D_{K^+} was calculated using eqn. 10.

$$D_{K^+} = \frac{4}{\pi t}\left(\frac{m_B V_m}{M_B S}\right)^2\left(\frac{\Delta E_s}{\Delta E_t}\right)^2 \tag{10}$$

Where t is the pulse duration (30 mins), m_B is the mass of active material in the electrode (g), S is the crosssection of the electrode (1.13 cm^2), M_B and V_m are molar mass (12 g/mol) and volume (8 cm^3/g) since the density of hard carbon is ~1.5 g/cm^3. (d=(m/V) = 8 (g/cm^3)) of the active material (hard Carbon) ΔE_s and ΔE_t are the change in potential during and after the current pulse [33]. Fig. 11a shows the IR drop and the change in voltage at the steady state (ΔE_s) and during the current pulse (ΔE_t). The calculated diffusion coefficients using equation 10 for potassiation and de-potassiation are given in Fig. 10 (c and d).

During potassiation (Fig. 10c), the calculated diffusion coefficient of KAP-1100 is 5×10^{-8} cm^2/s at higher voltages (above > 0.8 V vs. K/K^+). This high value indicates the ease of adsorption of K^+ ions. A linear decrease in the diffusion coefficient was observed further below 0.8 V vs. K/K^+ due to the electrostatic repulsion experienced on continuous insertion of K^+ into the nanographitic domains [83]. The lowest

Table 1
The electrochemical properties of reported hard carbon.

Sl. No	Raw material	Temp. (°C)	Procedure	BET-Specific surface area (m^2/g)	Initial specific capacity (mAh/g) @ current density (mA/g)	Cycling stability - reversible capacity (mAh/g) @ current dentsity (mA/g)	Cycles	Specific capacity (mAh/g) @ current density (mA/g)	Reference
1	Balsa Wood	800	Preoxidation	69.3	252.7 @ 100	233.1 @ 200	500	165@2000	[7]
2	Animal Bone	850	Precalcination	1474.5	470 @ 58(0.2C)	250 @ 58 (0.2C)	450	113@580 (2C)	[39]
3	N - Doped Sugarcane	800	Activation	466.21	142 @100	100 @ 200	400	20 @ 1000	[42]
4	Jute Fiber	1000	Microwave synthesis	516	153@60 (0.2 C)	116 @ 30 (0.1 C)	50	32@ 3000 (10 C)	[44]
5	Ficus Religiosa Leaf	900	Acid pretreatment		205 @20	76 @ 50	50	25 @ 280	[45]
6	Water Chestnut	900	Acid Pretreatment		243.8@100	220.5 @100	1000	134.8@ 1000	[46]
7	S-Doped Bamboo Derived Carbon	700	Hydrothermal	336.4	314 @50	87.41% @ 200		124.2 @ 1000	[47]
8	Rose Petals	1000	Preoxidaiton		236.2 @100	193.1 @500	800	134.6 @ 1000	[48]
9	N,P Doped Soybean	700	Direct carbonization	10.5	280 @ 1000	138 @ 2000	2000	179 @ 5000	[50]
10	O-Doped Orange Peel Derived Carbon	1000	Peroxidation	113.86	320 @50	79.5% @ 2000		134.6 @ 2000	[51]
11	Biopolymer (1% Cellulose Nanofibrils)	1000	Freeze drying	362.2	357 @ 100	180 @ 500	1000	170 @ 1000	[69]
12	Magnolia Grandiflora Lima	1200	Direct carbonization	95.7	240.6 @ 30	96.6@2000	2000	126.8 @ 2000	[98]
13	N-Doped Glucose Derived Carbon	900	Hydrothermal		251 @200	80% @ 200	600	93 @ 2000	[99]
14	Tremella	800	Molten salt	517	386.3 @ 100	122.9 @ 1000	1000	119.7@ 2000	[100]
15	Boron Doped Pine Cone Carbon	800	Molten salt	963	238.7 @50	115.9 @ 1000	2000	130.9 @ 1000	[101]
16	Masson Pine Trees	600	Molten salt		150.2 @50	71.6% @ 1000	700	64.4 @ 1000	[102]
17	***Kigelia Africana***	**1100**	**Direct carbonization**	**5.2**	**220@20**	**71 @ 200**	**200**	**32 @ 2000**	**This work**

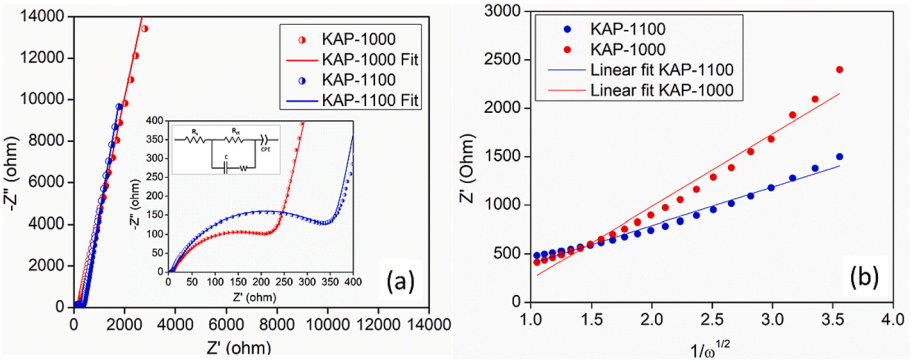

Fig. 9. (a) EIS spectra (Inset: enlarged version of the high-frequency region and the equivalent RC circuit) and (b) dependence of Z' with reciprocal of the square root of ω.

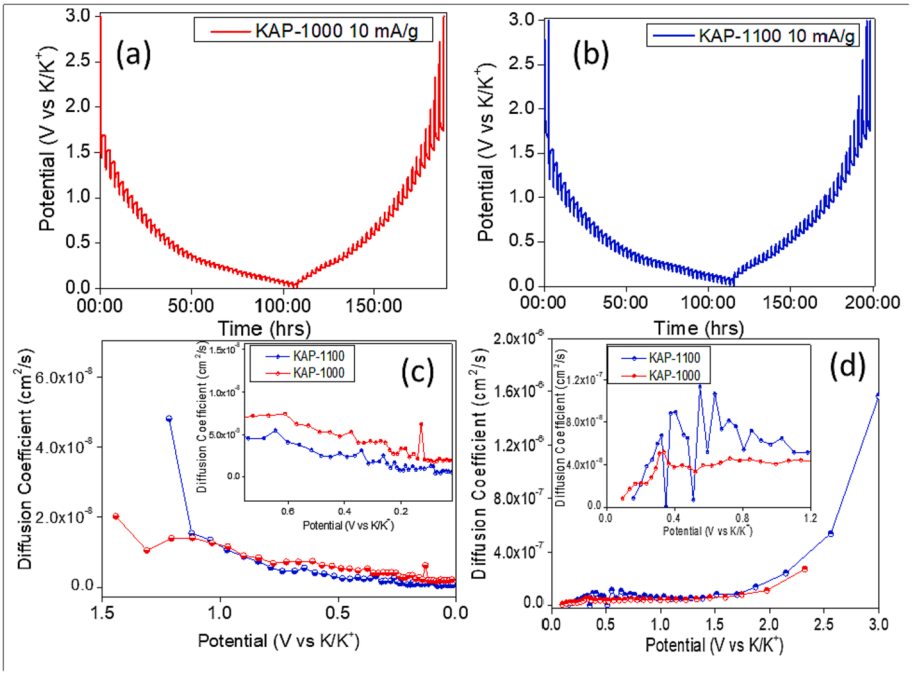

Fig. 10. (a,b) GITT cycle profile for KAP-1000 and KAP-1100 at 10 mA/g and (c, d) diffusion coefficient for KAP-1000 and KAP-1100 at 10 mA/g during potassiation and de-potassiation.

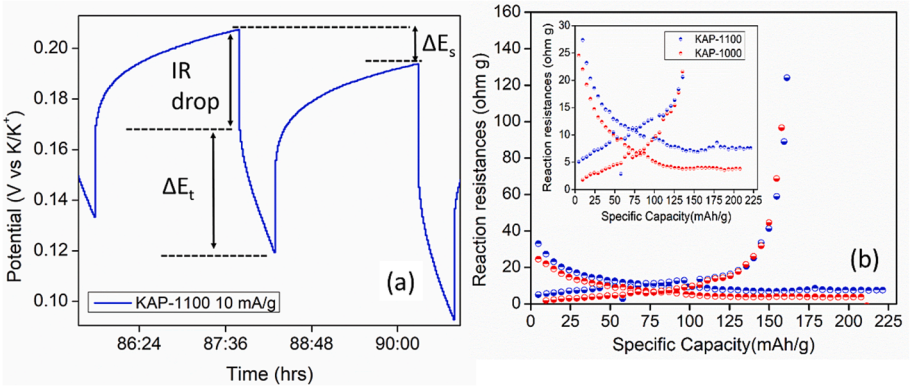

Fig. 11. (a) IR drop and change in potential during each pulse and (b) Reaction resistances calculated from the observed GITT profile.

diffusion coefficient of 0.2 × 10^{-8} cm^2/s of KAP-1100 indicates the difficulty with which the K^+ ions are inserted into the nanographitic domain [83,84,105].

Similarly, during de-potassiation (Fig. 10d), a stable region is observed, attributed to the de-insertion of K^+ from the domains. The characteristic increase in diffusion coefficient from 1 × 10^{-8} cm^2/s to

7×10^{-8} cm^2/s is due to the weakening of electrostatic repulsion. Further, a parabolic regime 6.5×10^{-7} cm^2/s to 1.6×10^{-6} cm^2/s) was observed with the release of accumulated K^+ charges from the low energy O-active sites on the surface at above 0.8 V vs K/K^+ [51]. Similar and close differences in diffusion coefficient were observed for KAP-1000, with approximately four times less diffusivity than the KAP-1100 infers from the well-grown nanographitic crystallites. This facilitated better K^+ ion diffusivity, even at the high voltage region above 1.5 V vs. K/K^+. Overall, KAP-1100 has better adsorption of K^+ ions than KAP-1000, as evident from both Fig. 10c and 10d.

In addition, the reaction resistances experienced by the electrode during the relaxation at equilibrium potentials are depicted in Fig. 11b. Usually, the overpotential in the K-ion batteries deduces the resistance of the active material at the desired voltages. The overpotential in the electrode gradually decreases during the potassiation (discharge) and increases gradually during the de-potassiation (charge). The reaction resistances are calculated by dividing the overpotential with the applied pulse current [106,107]. It can be seen that the reaction resistance is high in the high voltage region ~ 20 Ohm g (Fig. 11b). During the discharge, the gradual decrease in resistance to 1 Ohm g shows the contribution of the capacitive type charge transfer occurring from the disordered carbon. Likewise, a stable reduction in the resistance below 0.5 V vs K/K^+ region is entirely due to the increasing K-ion concentration in the electrode as it approaches 0.01 V vs K/K^+. The alkali metal ion insertion into graphitic crystallites enhances the contact between intergraphitic crystallites, resulting in better electrical conductivity on contact. In KAP-1100, a small increase in the reaction resistance on discharge/ reduction is due to the phase transformation that occurred; the accumulated stress in the region in Fig. 11b (inset) shows a small peak-like increase in reaction resistance from 7 to 9 Ohm g and then gradually decreasing to 7.3 Ohm g as the reaction progresses. Similar types of phase transitions could not be observed in KAP-1100, indicating the resistance experienced during insertion. Despite the continuous charge storage in the graphite-like layers, the stable reaction resistance resembles the charge storage by partial intercalation, indicating less stress induced on hard carbon on insertion. This further corroborates the b-values obtained around ~250 mV at different scan rates from CV. On de-insertion of K-ions, the decreasing concentration of K-ions in the anode leads to less electrical conductivity between nano-graphitic crystallite domains. Hence, as the phase transition progresses there is a high reaction resistance [108].

4. Conclusion

In summary, cellulose-rich *Kigelia Africana*-derived hard carbon is prepared by direct carbonization method at high temperatures. The formation of randomly oriented nano-graphitic crystallites by local ordering was confirmed by HRTEM analysis. The larger d-spacing than graphite and the low surface area controls the formation of SEI layer on the surface. The effect of temperature on the physical characteristics of the carbon on the degree of dis-orderness and graphitization was analyzed. Despite the lower surface area of 5.2 m^2/g, the presence of surface oxygen from XPS analysis and the formation of graphitic crystallites has shown significant differences in CV and GCD analysis. At low scan rates, the consecutive fading at around 0.25 V vs K/K^+ offers the passivation of the irreversible loss of K-ion at the electrode to the SEI layer. KAP carbonized at 1100 °C shows better rate capability with a reversible 180 and 68 mAh/g capacity at 50 and 500 mA/g. The CV, GITT, and EIS confirmed that the diffusion of K-ions in the prepared hard carbon has a maximum capacitive dominant contribution and the insertion capacity in the nanographitic crystallites. The smaller quasi-plateau region at low voltages corresponds to the pseudo-graphitic domains obtained at elevated temperatures. The local ordering responsible for the formation of nanographititc crystallites resistive to structural transformation on intercalation of K-ions upon insertion played a major role in KAP-1100 for better performance. Therefore, the direct pyrolysis method could elevate the internal structural properties of the biomass for better electrochemical characteristics without any pretreatment.

CRediT authorship contribution statement

N. Prasanna Naga Puneeth: . **K. Rajkumar:** Conceptualization, Data curation, Formal analysis, Methodology, Investigation, Writing – original draft. **A. Soundarya:** Investigation, Methodology. **S.D. Kaushik:** . **Yun Sung Lee:** . **Sangho Park:** Resources. **R. Kalai Selvan:** Conceptualization, Formal analysis, Writing – review & editing, Supervision, Funding acquisition.

Declaration of competing interest

The authors declare that they have no known competing financial interests or personal relationships that could have appeared to influence the work reported in this paper.

Data availability

Data will be made available on request.

Acknowledgments

The work is financially supported by the UGC-DAE Consortium for Scientific Research (CRS – M – 309). The authors greatly acknowledge DST-FIST and DST-SERB for establishing Glove box and battery cycler facilities at ESCD Lab, Bharathiar University. The authors also happy to acknowledge the Central Instrumentation Centre, Bharathiar University, Coimbatore (CIC, BU), and the DST PURSE (Phase II) program for the HR-TEM analysis.

References

[1] L. Fan, R. Ma, Q. Zhang, X. Jia, B. Lu, Graphite anode for a potassium-ion battery with unprecedented performance, Angew. Chem. 131 (31) (2019) 10610–10615.
[2] C. Liu, H. Zheng, Y. Wang, N. Xiao, K. Yu, H. Li, X. Zhang, H. Bai, T. Ma, J. Qiu, Microstructure regulation of pitch-based soft carbon anodes by iodine treatment towards high-performance potassium-ion batteries, J. Colloid Interface Sci. 615 (2022) 485–493.
[3] W.-J. Deng, X.-D. He, L.-M. Zhang, J.-R. Wang, C.-H. Chen, Highly graphitic N-doped biomass-derived hard carbon with a low operating potential for potassium-ion batteries, Energ. Technol. 9 (12) (2021) 2100644.
[4] U. Kumar, J. Wu, N. Sharma, V. Sahajwalla, Biomass derived high areal and specific capacity hard carbon anodes for sodium-ion batteries, Energy Fuel 35 (2) (2021) 1820–1830.
[5] V. Simone, A. Boulineau, A. De Geyer, D. Rouchon, L. Simonin, S. Martinet, Hard carbon derived from cellulose as anode for sodium ion batteries: Dependence of electrochemical properties on structure, J. Energy Chem. 25 (5) (2016) 761–768.
[6] Z. Wu, J. Zou, Y. Zhang, X. Lin, D. Fry, L. Wang, J. Liu, Lignin-derived hard carbon anode for potassium-ion batteries: Interplay among lignin molecular weight, material structures, and storage mechanisms, Chem. Eng. J. 427 (2022), 131547.
[7] W. Yu, Z. Liu, X. Yu, B. Lu, Balsa-wood-derived binder-free freestanding carbon foam as high-performance potassium anode, Adv. Energy Sustainability Res. 2 (6) (2021) 2100018.
[8] C. Zhou, A. Li, B. Cao, X. Chen, M. Jia, H. Song, The non-ignorable impact of surface oxygen groups on the electrochemical performance of N/O dual-doped carbon anodes for sodium ion batteries, J. Electrochem. Soc. 165 (7) (2018) A1447.
[9] Q. Yang, Z. Wang, W. Xi, G. He, Tailoring nanoporous structures of Ge anodes for stable potassium-ion batteries, Electrochem. Commun. 101 (2019) 68–72.
[10] Z. Sang, D. Su, J. Wang, Y. Liu, H. Ji, Bi-continuous nanoporous carbon sphere derived from SiOC as high-performance anodes for PIBs, Chem. Eng. J. 381 (2020), 122677.
[11] Z. Ma, Q. Li, H. Pang, Z. Yu, D. Yan, $Ti_3C_2T_x$@ $K_2Ti_4O_9$ composite materials by controlled oxidation and alkalization strategy for potassium ion batteries, Ceram. Int. 48 (11) (2022) 16418–16424.
[12] X. Li, J. Li, L. Ma, C. Yu, Z. Ji, L. Pan, W. Mai, Graphite anode for potassium ion batteries: current status and perspective, Energy Environ. Mater. 5 (2) (2022) 458–469.
[13] Y. Zhao, L. Yang, C. Ma, G. Han, One-step fabrication of fluorine-doped graphite derived from a low-grade microcrystalline graphite ore for potassium-ion batteries, Energy Fuel 34 (7) (2020) 8993–9001.

[14] Z. Ma, Y. Gao, C. Bao, X. Xia, H. Liu, Reasonable intrinsic microstructure of microcrystalline graphite for high-rate and long-life potassium-ion batteries, Electrochim. Acta 440 (2023), 141703.
[15] L. Wang, J. Yang, J. Li, T. Chen, S. Chen, Z. Wu, J. Qiu, B. Wang, P. Gao, X. Niu, Graphite as a potassium ion battery anode in carbonate-based electrolyte and ether-based electrolyte, J. Power Sources 409 (2019) 24–30.
[16] X. Li, Y. Lei, L. Qin, D. Han, H. Wang, D. Zhai, B. Li, F. Kang, Mildly-expanded graphite with adjustable interlayer distance as high-performance anode for potassium-ion batteries, Carbon 172 (2021) 200–206.
[17] L.F. Zhao, Z. Hu, W.H. Lai, Y. Tao, J. Peng, Z.C. Miao, Y.X. Wang, S.L. Chou, H. K. Liu, S.X. Dou, Hard carbon anodes: fundamental understanding and commercial perspectives for Na-ion batteries beyond Li-ion and K-ion counterparts, Adv. Energy Mater. 11 (1) (2021) 2002704.
[18] C. Chen, M. Wu, Y. Wang, K. Zaghib, Insights into pseudographite-structured hard carbon with stabilized performance for high energy K-ion storage, J. Power Sources 444 (2019), 227310.
[19] J. Zhang, L. Lai, H. Wang, M. Chen, Z. Shen, Energy storage mechanisms of anode materials for potassium ion batteries, Mater. Today Energy 21 (2021), 100747.
[20] H. Lei, J. Li, X. Zhang, L. Ma, Z. Ji, Z. Wang, L. Pan, S. Tan, W. Mai, A review of hard carbon anode: Rational design and advanced characterization in potassium ion batteries, InfoMat 4 (2) (2022) e12272.
[21] J. Touja, V. Gabaudan, F. Farina, S. Cavaliere, L. Caracciolo, L. Madec, H. Martinez, A. Boulaoued, J. Wallenstein, P. Johansson, Self-supported carbon nanofibers as negative electrodes for K-ion batteries: Performance and mechanism, Electrochim. Acta 362 (2020), 137125.
[22] T. Zhang, J. Mao, X. Liu, M. Xuan, K. Bi, X.L. Zhang, J. Hu, J. Fan, S. Chen, G. Shao, Pinecone biomass-derived hard carbon anodes for high-performance sodium-ion batteries, RSC Adv. 7 (66) (2017) 41504–41511.
[23] K. Kubota, S. Shimadzu, N. Yabuuchi, S. Tominaka, S. Shiraishi, M. Abreu-Sepulveda, A. Manivannan, K. Gotoh, M. Fukunishi, M. Dahbi, Structural analysis of sucrose-derived hard carbon and correlation with the electrochemical properties for lithium, sodium, and potassium insertion, Chem. Mater. 32 (7) (2020) 2961–2977.
[24] D.R. Kumar, I. Kanagaraj, G. Dhakal, A. Prakash, J.-J. Shim, Palmyra palm tree biomass-derived carbon low-voltage plateau region capacity on Na-ion battery and its full cell performance, J. Environ. Chem. Eng. 9 (4) (2021), 105698.
[25] M. Dahbi, M. Kiso, K. Kubota, T. Horiba, T. Chafik, K. Hida, T. Matsuyama, S. Komaba, Synthesis of hard carbon from argan shells for Na-ion batteries, J. Mater. Chem. A 5 (20) (2017) 9917–9928.
[26] M. Yang, Q. Kong, W. Feng, W. Yao, N/O double-doped biomass hard carbon material realizes fast and stable potassium ion storage, Carbon 176 (2021) 71–82.
[27] C.d.M. Saavedra Rios, L. Simonin, A.d. Geyer, C. Matei Ghimbeu, C. Dupont, Unraveling the properties of biomass-derived hard carbons upon thermal treatment for a practical application in na-ion batteries, Energies 13 (14) (2020) 3513.
[28] A. Beda, J.-M. Le Meins, P.-L. Taberna, P. Simon, C.M. Ghimbeu, Impact of biomass inorganic impurities on hard carbon properties and performance in Na-ion batteries, Sustain. Mater. Technol. 26 (2020) e00227.
[29] X. He, J. Liao, Z. Tang, L. Xiao, X. Ding, Q. Hu, Z. Wen, C. Chen, Highly disordered hard carbon derived from skimmed cotton as a high-performance anode material for potassium-ion batteries, J. Power Sources 396 (2018) 533–541.
[30] H.D. Pham, J.F. Fernando, M. Horn, J. MacLeod, N. Motta, W.O. Doherty, A. Payne, A.K. Nanjundan, D. Golberg, D. Dubal, Multi-heteroatom doped nanocarbons for high performance double carbon potassium ion capacitor, Electrochim. Acta 389 (2021), 138717.
[31] C. Gao, Q. Wang, S. Luo, Z. Wang, Y. Zhang, Y. Liu, A. Hao, R. Guo, High performance potassium-ion battery anode based on biomorphic N-doped carbon derived from walnut septum, J. Power Sources 415 (2019) 165–171.
[32] W. Li, Z. Li, C. Zhang, W. Liu, C. Han, B. Yan, S. An, X. Qiu, Hard carbon derived from rice husk as anode material for high performance potassium-ion batteries, Solid State Ion. 351 (2020), 115319.
[33] Z. Wu, L. Wang, J. Huang, J. Zou, S. Chen, H. Cheng, C. Jiang, P. Gao, X. Niu, Loofah-derived carbon as an anode material for potassium ion and lithium ion batteries, Electrochim. Acta 306 (2019) 446–453.
[34] W. Cao, E. Zhang, J. Wang, Z. Liu, J. Ge, X. Yu, H. Yang, B. Lu, Potato derived biomass porous carbon as anode for potassium ion batteries, Electrochim. Acta 293 (2019) 364–370.
[35] S. Chen, K. Tang, F. Song, Z. Liu, N. Zhang, S. Lan, X. Xie, Z. Wu, Porous hard carbon spheres derived from biomass for high-performance sodium/potassium-ion batteries, Nanotechnology 33 (5) (2021), 055401.
[36] R. Verma, Y.N. Singhbabu, P.N. Didwal, A.G. Nguyen, J. Kim, C.J. Park, Biowaste orange peel-derived mesoporous carbon as a cost-effective anode material with ultra-stable cyclability for potassium-ion batteries, Batteries & Supercaps 3 (10) (2020) 1099–1111.
[37] P. Wang, Z. Gong, K. Zhu, K. Ye, J. Yan, J. Yin, G. Wang, D. Cao, Nano-phosphorus supported on biomass carbon by gas deposition as negative electrode material for potassium ion batteries, Electrochim. Acta 362 (2020), 137153.
[38] P. Wang, Z. Gong, K. Ye, Y. Gao, K. Zhu, J. Yan, G. Wang, D. Cao, N-rich biomass carbon derived from hemp as a full carbon-based potassium ion hybrid capacitor anode, Appl. Surf. Sci. 553 (2021), 149569.
[39] X. Yuan, B. Zhu, J. Feng, C. Wang, X. Cai, R. Qin, Biomass bone-derived, N/P-doped hierarchical hard carbon for high-energy potassium-ion batteries, Mater. Res. Bull. 139 (2021), 111282.
[40] Q. Wang, C. Gao, W. Zhang, S. Luo, M. Zhou, Y. Liu, R. Liu, Y. Zhang, Z. Wang, A. Hao, Biomorphic carbon derived from corn husk as a promising anode materials for potassium ion battery, Electrochim. Acta 324 (2019), 134902.
[41] M. Yang, Q. Kong, W. Feng, W. Yao, Q. Wang, Hierarchical porous nitrogen, oxygen, and phosphorus ternary doped hollow biomass carbon spheres for high-speed and long-life potassium storage, Carbon Energy 4 (1) (2022) 45–59.
[42] Q. Deng, H. Liu, Y. Zhou, Z. Luo, Y. Wang, Z. Zhao, R. Yang, N-doped three-dimensional porous carbon materials derived from bagasse biomass as an anode material for K-ion batteries, J. Electroanal. Chem. 899 (2021), 115668.
[43] T. Zhu, B. Mai, P. Hu, C. Cai, B. Xing, Z. Wei, C. Chen, H. Fan, M. Li, X. Wang, Bagasse-derived hard carbon anode with an adsorption-intercalation mechanism for high-rate potassium storage, ACS Appl. Energy Mater. 6 (4) (2023) 2370–2377.
[44] Nagmani, P. Verma, S. Puravankara, Jute-fiber precursor-derived low-cost sustainable hard carbon with varying micro/mesoporosity and distinct storage mechanisms for sodium-ion and potassium-ion batteries, Langmuir 38 (50) (2022) 15703–15713.
[45] K. Rajkumar, M. Ragupathi, Y.S. Lee, R.K. Selvan, Preparation of sponge-like porous carbon from Ficus Religiosa leaf and its K-ion intercalation properties, Mater. Lett. 301 (2021), 130298.
[46] Z. Xu, S. Du, Z. Yi, J. Han, C. Lai, Y. Xu, X. Zhou, Water chestnut-derived slope-dominated carbon as a high-performance anode for high-safety potassium-ion batteries, ACS Appl. Energy Mater. 3 (11) (2020) 11410–11417.
[47] S. Tian, D. Guan, J. Lu, Y. Zhang, T. Liu, X. Zhao, C. Yang, J. Nan, Synthesis of the electrochemically stable sulfur-doped bamboo charcoal as the anode material of potassium-ion batteries, J. Power Sources 448 (2020), 227572.
[48] Z. Hu, Z. Liu, J. Zhao, X. Yu, B. Lu, Rose-petals-derived hemispherical micropapillae carbon with cuticular folds for super potassium storage, Electrochim. Acta 368 (2021), 137629.
[49] J.-F. Lu, K.-C. Li, X.-Y. Lv, H.-X. Kuai, J. Su, Y.-X. Wen, Boron-doped pine-cone carbon with 3D interconnected porosity for use as an anode for potassium-ion batteries with long life cycle, Front. Chem. 10 (2022), 953782.
[50] S. Tao, W. Xu, J. Zheng, F. Kong, P. Cui, D. Wu, B. Qian, S. Chen, L. Song, Soybean roots-derived N, P co-doped mesoporous hard carbon for boosting sodium and potassium-ion batteries, Carbon 178 (2021) 233–242.
[51] K. Zhao, C. Chen, M. La, C. Yang, O-doping configurations reduce the adsorption energy barrier of k-ions to improve the electrochemical performance of biomass-derived carbon, Micromachines 13 (5) (2022) 806.
[52] R. Siva, T. Valarmathi, K. Palanikumar, A.V. Samrot, Study on a Novel natural cellulosic fiber from Kigelia africana fruit: characterization and analysis, Carbohydr. Polym. 244 (2020), 116494.
[53] K. Singh, M. Gautam, B. Chandra, A. Kumar, Removal of Pb (II) from its aqueous solution by activated carbon derived from Balam Khira (Kigelia Africana), Desalin. Water Treat. 57 (51) (2016) 24487–24497.
[54] H. Kaur, R. Shyam, R. Amutha, Kigelia africana fruit carbon as a low cost adsorbent for removal of copper (II) ions from aqueous solution, Nat. Environ. Pollut. Technol. 10 (3) (2011) 419–422.
[55] J.F. Amaku, S.A. Ogundare, K.G. Akpomie, J. Conradie, Enhanced sequestration of Cr (VI) onto plant extract anchored on carbon-coated aluminium oxide composite, Environ. Sci. Pollut. Res. 28 (2021) 57723–57738.
[56] V. Yadav, D. Tiwari, M. Bhagat, Activated carbon of Kigelia africana as bio-adsorbent: synthesis and characterization, Int. J. Res. Anal. Rev. 6 (2019) 958–964.
[57] V. Yadav, D. Tiwari, M. Bhagat, Arsenic removal using chemically modified Kigelia Africana as a low-cost bio-adsorbent: equilibrium, kinetics and thermodynamics studies, Int. J. Basic Appl. Res 9 (2019) 1282–1294.
[58] P.G. Kumar, V. Vigneswaran, V. Sivalingam, R. Velraj, S.C. Kim, V. Ramkumar, Enhancing heat transfer performance of automotive radiator with H2O/activated carbon nanofluids, J. Mol. Liq. 371 (2023), 121153.
[59] Y. Jin, Z. Shi, T. Han, H. Yang, H.D. Asfaw, R. Gond, R. Younesi, P.G. Jönsson, W. Yang, From waste biomass to hard carbon anodes: predicting the relationship between biomass processing parameters and performance of hard carbons in sodium-ion batteries, Processes 11 (3) (2023) 764.
[60] H. Lu, F. Ai, Y. Jia, C. Tang, X. Zhang, Y. Huang, H. Yang, Y. Cao, Exploring sodium-ion storage mechanism in hard carbons with different microstructure prepared by ball-milling method, Small 14 (39) (2018) 1802694.
[61] K. Wang, Y. Jin, S. Sun, Y. Huang, J. Peng, J. Luo, Q. Zhang, Y. Qiu, C. Fang, J. Han, Low-cost and high-performance hard carbon anode materials for sodium-ion batteries, ACS Omega 2 (4) (2017) 1687–1695.
[62] S. Shanmugapriya, P.R. Kasturi, P. Zhu, J. Zhu, C. Yan, X. Zhang, R.K. Selvan, Hexanedioic acid mediated in situ functionalization of interconnected graphitic 3D carbon nanofibers as Pt support for trifunctional electrocatalysts, Sustainable Energy Fuels 4 (6) (2020) 2808–2822.
[63] M. Song, Z. Yi, R. Xu, J. Chen, J. Cheng, Z. Wang, Q. Liu, Q. Guo, L. Xie, C. Chen, Towards enhanced sodium storage of hard carbon anodes: Regulating the oxygen content in precursor by low-temperature hydrogen reduction, Energy Storage Mater. 51 (2022) 620–629.
[64] F. Sun, H. Wang, Z. Qu, K. Wang, L. Wang, J. Gao, J. Gao, S. Liu, Y. Lu, Carboxyl-dominant oxygen rich carbon for improved sodium ion storage: synergistic enhancement of adsorption and intercalation mechanisms, Adv. Energy Mater. 11 (1) (2021) 2002981.
[65] H. Wang, F. Sun, Z. Qu, K. Wang, L. Wang, X. Pi, J. Gao, G. Zhao, Oxygen functional group modification of cellulose-derived hard carbon for enhanced sodium ion storage, ACS Sustain. Chem. Eng. 7 (22) (2019) 18554–18565.

[66] N. Zhao, C. Wang, B. Li, W. Shen, F. Kang, Z.-H. Huang, Construction of flexible lignin/polyacrylonitrile-based carbon nanofibers for dual-carbon sodium-ion capacitors, J. Mater. Sci. 57 (25) (2022) 11809–11823.

[67] X. Lin, Y. Liu, H. Tan, B. Zhang, Advanced lignin-derived hard carbon for Na-ion batteries and a comparison with Li and K ion storage, Carbon 157 (2020) 316–323.

[68] M. Kakunuri, C.S. Sharma, Candle soot derived fractal-like carbon nanoparticles network as high-rate lithium ion battery anode material, Electrochim. Acta 180 (2015) 353–359.

[69] Y. Feng, K. Wu, S. Wu, M. He, X. Xu, M. Xue, In situ oxygen-doped porous carbon nanoribbons with expanded interlayer distance for enhanced potassium ion storage, ACS Appl. Energy Mater. 5 (10) (2022) 12966–12976.

[70] H. Zhang, H. Ming, W. Zhang, G. Cao, Y. Yang, Coupled carbonization strategy toward advanced hard carbon for high-energy sodium-ion battery, ACS Appl. Mater. Interfaces 9 (28) (2017) 23766–23774.

[71] B. Yang, J. Wang, Y. Zhu, K. Ji, C. Wang, D. Ruan, Y. Xia, Engineering hard carbon with high initial coulomb efficiency for practical sodium-ion batteries, J. Power Sources 492 (2021), 229656.

[72] A. Gomez-Martin, J. Martinez-Fernandez, M. Ruttert, M. Winter, T. Placke, J. Ramirez-Rico, Correlation of structure and performance of hard carbons as anodes for sodium ion batteries, Chem. Mater. 31 (18) (2019) 7288–7299.

[73] C. Wang, J. Huang, J. Li, L. Cao, Q. Chen, C. Qian, S. Chen, Revealing the effect of nanopores in biomass-derived carbon on its sodium-ion storage behavior, ChemElectroChem 7 (1) (2020) 201–211.

[74] P.K. Mubari, T. Beguerie, M. Monthioux, E. Weiss-Hortala, A. Nzihou, P. Puech, The X-ray, Raman and TEM signatures of cellulose-derived carbons explained, C 8 (1) (2022) 4.

[75] P. Mallet-Ladeira, P. Puech, C. Toulouse, M. Cazayous, N. Ratel-Ramond, P. Weisbecker, G.L. Vignoles, M. Monthioux, A Raman study to obtain crystallite size of carbon materials: a better alternative to the Tuinstra-Koenig law, Carbon 80 (2014) 629–639.

[76] E.M. Lotfabad, J. Ding, K. Cui, A. Kohandehghan, W.P. Kalisvaart, M. Hazelton, D. Mitlin, High-density sodium and lithium ion battery anodes from banana peels, ACS Nano 8 (7) (2014) 7115–7129.

[77] A.K. Nanjundan, R.R. Gaddam, A.H. Farokh Niaei, P.K. Annamalai, D.P. Dubal, D. J. Martin, Y. Yamauchi, D.J. Searles, X.S. Zhao, Potassium-Ion Storage in Cellulose-Derived Hard Carbon: The Role of Functional Groups, Batteries & Supercaps 3(9) (2020) 953–960.

[78] B. Dippel, H. Jander, J. Heintzenberg, NIR FT Raman spectroscopic study of flame soot, Phys. Chem. Chem. Phys. 1 (20) (1999) 4707–4712.

[79] H.D. Asfaw, R. Gond, A. Kotronia, C.-W. Tai, R. Younesi, Bio-derived hard carbon nanosheets with high rate sodium-ion storage characteristics, Sustain. Mater. Technol. 32 (2022) e00407.

[80] T.K. Kumaresan, S.A. Masilamani, K. Raman, S.Z. Karazhanov, R. Subashchandrabose, High performance sodium-ion battery anode using biomass derived hard carbon with engineered defective sites, Electrochim. Acta 368 (2021), 137574.

[81] J.L. Xia, D. Yan, L.P. Guo, X.L. Dong, W.C. Li, A.H. Lu, Hard carbon nanosheets with uniform ultramicropores and accessible functional groups showing high realistic capacity and superior rate performance for sodium-ion storage, Adv. Mater. 32 (21) (2020) 2000447.

[82] U. Mittal, L. Djuandhi, N. Sharma, H.L. Andersen, Structure and function of hard carbon negative electrodes for sodium-ion batteries, J. Phys.: Energy 4 (4) (2022), 042001.

[83] Y. Tian, X. Zhu, M. Abbas, D.W. Tague, J.P. Ferraris, K.J. Balkus Jr., Two-dimensional hexagonal-shaped mesoporous carbon sheets for supercapacitors, ACS Omega 7 (32) (2022) 27896–27902.

[84] Y. Tian, X. Zhu, M. Abbas, D.W. Tague, M.A. Wunch, J.P. Ferraris, K.J. Balkus, Magnesium hydroxide templated hierarchical porous carbon nanosheets as electrodes for high-energy-density supercapacitors, ACS Appl. Energy Mater. 5 (6) (2022) 6805–6813.

[85] L. Larbi, B. Larhrib, A. Beda, L. Madec, L. Monconduit, C. Matei Ghimbeu, Impact of hard carbon properties on their performance in potassium-ion batteries, ACS Appl. Energy Mater. 6 (10) (2023) 5274–5289.

[86] N. Cheng, W. Zhou, J. Liu, Z. Liu, B. Lu, Reversible oxygen-rich functional groups grafted 3D honeycomb-like carbon anode for super-long potassium ion batteries, Nano-Micro Letters 14 (1) (2022) 1–15.

[87] Y. Zhu, M. Wang, Y. Zhang, R. Wang, Y. Zhang, C. Wang, Nitrogen/oxygen dual-doped hierarchically porous carbon/graphene composite as high-performance anode for potassium storage, Electrochim. Acta 377 (2021), 138093.

[88] G. Shi, Z. Han, L. Hu, B. Wang, F. Huang, N/O Co-doped hard carbon derived from cocklebur fruit for sodium-ion storage, ChemElectroChem 9 (8) (2022) e202200138.

[89] M. Scardamaglia, T. Susi, C. Struzzi, R. Snyders, G. Di Santo, L. Petaccia, C. Bittencourt, Spectroscopic observation of oxygen dissociation on nitrogen-doped graphene, Sci. Rep. 7 (1) (2017) 7960.

[90] V. Thirumal, T. Sreekanth, K. Yoo, J. Kim, Biomass-derived hard carbon and nitrogen-sulfur co-doped graphene for high-performance symmetric sodium ion capacitor devices, Energies 16 (2) (2023) 802.

[91] J. Xu, C. Fan, M. Ou, S. Sun, Y. Xu, Y. Liu, X. Wang, Q. Li, C. Fang, J. Han, Correlation between potassium-ion storage mechanism and local structural evolution in hard carbon materials, Chem. Mater. 34 (9) (2022) 4202–4211.

[92] L. Larbi, B. Larhrib, A. Beda, L.n.c. Madec, L. Monconduit, C. Matei Ghimbeu, Impact of hard carbon properties on their performance in potassium-ion batteries, ACS Appl. Energy Mater. (2023).

[93] Z. Xing, Y. Qi, Z. Jian, X. Ji, Polynanocrystalline graphite: a new carbon anode with superior cycling performance for K-ion batteries, ACS Appl. Mater. Interfaces 9 (5) (2017) 4343–4351.

[94] F. Yuan, D. Zhang, Z. Li, H. Sun, Q. Yu, Q. Wang, J. Zhang, Y. Wu, K. Xi, B. Wang, Unraveling the intercorrelation between micro/mesopores and K migration behavior in hard carbon, Small 18 (12) (2022) 2107113.

[95] M. Yang, J. Dai, M. He, T. Duan, W. Yao, Biomass-derived carbon from Ganoderma lucidum spore as a promising anode material for rapid potassium-ion storage, J. Colloid Interface Sci. 567 (2020) 256–263.

[96] Z. Liu, S. Wu, Y. Song, T. Yang, Z. Ma, X. Tian, Z. Liu, Non-negligible influence of oxygen in hard carbon as an anode material for potassium-ion batteries, ACS Appl. Mater. Interfaces 14 (42) (2022) 47674–47684.

[97] X. Zhang, R. Huang, F. Wu, R. Chen, L. Li, Mixed-biomass engineering achieves multi-doped highly-disordered hierarchical flower-like hard carbon for advanced potassium-ion battery, Nano Energy 117 (2023), 108913.

[98] Z. Zhu, W. Zhong, Y. Zhang, P. Dong, S. Sun, Y. Zhang, X. Li, Elucidating electrochemical intercalation mechanisms of biomass-derived hard carbon in sodium-/potassium-ion batteries, Carbon Energy 3 (4) (2021) 541–553.

[99] C. Chen, K. Zhao, M. La, C. Yang, Insight into a nitrogen-doping mechanism in a hard-carbon-microsphere anode material for the long-term cycling of potassium-ion batteries, Materials 15 (12) (2022) 4249.

[100] L. Zhu, Z. Zhang, H. Zhang, Y. Wang, J. Luo, J. Yu, Y. Qu, Z. Yang, Tunable 2D tremella-derived carbon nanosheets with enhanced pseudocapacitance behavior for ultrafast potassium-ion storage, Sci. China Technol. Sci. 64 (9) (2021) 2047–2056.

[101] J.-F. Lu, K.-C. Li, X.-Y. Lv, H.-X. Kuai, J. Su, Y.-X. Wen, Boron-doped pine-cone carbon with 3D interconnected porosity for use as an anode for potassium-ion batteries with long life cycle, Front. Chem. 10 (2022).

[102] J.-F. Lu, H.-X. Kuai, S.-S. Li, X.-Y. Lv, Y.-X. Wen, F.-H. Lei, Tuning the structure and electrochemical performance of pinecone-derived porous carbon for potassium-ion battery anodes using molten $ZnCl_2$, Ionics 28 (8) (2022) 3799–3816.

[103] C. Ge, Z. Fan, J. Zhang, Y. Qiao, J. Wang, L. Ling, Novel hard carbon/graphite composites synthesized by a facile in situ anchoring method as high-performance anodes for lithium-ion batteries, RSC Adv. 8 (60) (2018) 34682–34689.

[104] P. Yu, B.N. Popov, J.A. Ritter, R.E. White, Determination of the lithium ion diffusion coefficient in graphite, J. Electrochem. Soc. 146 (1) (1999) 8.

[105] R.F. Susanti, S. Alvin, J. Kim, Toward high-performance hard carbon as an anode for sodium-ion batteries: Demineralization of biomass as a critical step, J. Ind. Eng. Chem. 91 (2020) 317–329.

[106] Y. Xu, Y. Zhu, Y. Liu, C. Wang, Electrochemical performance of porous carbon/tin composite anodes for sodium-ion and lithium-ion batteries, Adv. Energy Mater. 3 (1) (2013) 128–133.

[107] J. Kim, S. Park, S. Hwang, W.-S. Yoon, Principles and applications of galvanostatic intermittent titration technique for lithium-ion batteries, J. Electrochem. Sci. Technol. 13 (1) (2021) 19–31.

[108] J. Zhao, X. Zou, Y. Zhu, Y. Xu, C. Wang, Electrochemical intercalation of potassium into graphite, Adv. Funct. Mater. 26 (44) (2016) 8103–8110.